



Multiphoton dissociation dynamics of the indenyl radical at 248 nm and 193 nm

Cite as: J. Chem. Phys. **151**, 174303 (2019); <https://doi.org/10.1063/1.5121294>

Submitted: 23 July 2019 . Accepted: 10 October 2019 . Published Online: 04 November 2019

Erin N. Sullivan , Bethan Nichols, Stephen von Kugelgen, Gabriel da Silva , and Daniel M. Neumark 



View Online



Export Citation



CrossMark

ARTICLES YOU MAY BE INTERESTED IN

[Theory of ultrafast x-ray scattering by molecules in the gas phase](#)

The Journal of Chemical Physics **151**, 174302 (2019); <https://doi.org/10.1063/1.5110040>

[Threshold photodissociation dynamics of NO₂ studied by time-resolved cold target recoil ion momentum spectroscopy](#)

The Journal of Chemical Physics **151**, 174301 (2019); <https://doi.org/10.1063/1.5095430>

[Engineering nonlinear response of superconducting niobium microstrip resonators via aluminum cladding](#)

Journal of Applied Physics **126**, 173906 (2019); <https://doi.org/10.1063/1.5121758>

Lock-in Amplifiers
... and more, from DC to 600 MHz



Multiphoton dissociation dynamics of the indenyl radical at 248 nm and 193 nm

Cite as: J. Chem. Phys. 151, 174303 (2019); doi: 10.1063/1.5121294

Submitted: 23 July 2019 • Accepted: 10 October 2019 •

Published Online: 4 November 2019



Erin N. Sullivan,¹  Bethan Nichols,^{1,a)} Stephen von Kugelgen,^{1,b)} Gabriel da Silva,² 
and Daniel M. Neumark^{1,c)} 

AFFILIATIONS

¹Department of Chemistry, University of California, Berkeley, California 94720, USA and Chemical Sciences Division, Lawrence Berkeley National Laboratory, Berkeley, California 94720, USA

²Department of Chemical Engineering, University of Melbourne, Victoria 3010 Australia

^{a)}Present address: Thumbtack, San Francisco, CA 94103, USA.

^{b)}Present address: Department of Chemistry, Northwestern University, Evanston, IL 60208, USA.

^{c)}Author to whom correspondence should be addressed: dneumark@berkeley.edu

ABSTRACT

Photofragment translational spectroscopy is used to investigate the unimolecular photodissociation of the indenyl radical (C_9H_7). C_9H_7 radicals are generated by photodetachment of $C_9H_7^-$ anions and are dissociated at 248 nm (5.00 eV) and 193 nm (6.42 eV). The following product channels are definitively observed at both wavelengths: $C_2H_2 + C_7H_5$, $C_2H_2 + C_3H_3 + C_4H_2$, and $C_2H_2 + C_2H_2 + C_5H_3$. The three-body product channels are energetically inaccessible from single photon excitation at either dissociation wavelength. This observation, in combination with calculated dissociation rates and laser power studies, implies that all dissociation seen in this experiment occurs exclusively through multiphoton processes in which the initial C_9H_7 radical absorbs two photons sequentially prior to dissociation to two or three fragments. The corresponding translational energy distributions for each product channel peak well below the maximum available energy for two photons and exhibit similar behavior regardless of dissociation wavelength. These results suggest that all products are formed by internal conversion to the ground electronic state, followed by dissociation.

Published under license by AIP Publishing. <https://doi.org/10.1063/1.5121294>

I. INTRODUCTION

Polycyclic aromatic hydrocarbons (PAHs) are compounds found in environments ranging from aerosols¹ to the interstellar medium.² The term PAH encompasses a wide range of chemical systems, including the indenyl radical (C_9H_7 ; Fig. 1), which play a role in soot formation, leading to adverse environmental and human health effects.^{3,4} While numerous smaller cyclic hydrocarbon radicals (C_5H_5 , C_6H_5 , for example) have been the subject of a variety of experiments to examine their broader reactivity, structure, and relevance,^{5,6} less attention has been devoted to C_9H_7 despite its likely importance in reactive pathways of larger PAHs.^{7,8} In this study, we examine the photochemistry of indenyl, a resonance-stabilized radical, via fast radical beam photodissociation in order to understand more about its unimolecular dynamics subsequent to UV excitation at 248 nm and 193 nm.

The electronic absorption spectrum of C_9H_7 has been measured in a 3-methylhexane matrix.⁹ The spectrum exhibits a strong feature at 415 nm in addition to some less intense structure down to about 350 nm, but no results at lower wavelengths were reported. The electron affinity of C_9H_7 was first measured by Römer *et al.*¹⁰ and was later refined by Kim and co-workers¹¹ to be 1.8019 eV via slow electron velocity map imaging; this same work observed detachment from the anion to the first electronic state of the neutral with a term energy of 0.95 eV. The ionization energy has been determined most recently by Hemberger *et al.*¹² using threshold photoionization spectroscopy and found to be 7.53 eV, substantially lower than the previously reported value of 8.35 eV.¹³

Indene (C_9H_8), indenyl (C_9H_7), and other isomers of C_9H_7 have been implicated as intermediates in PAH formation through the association of acetylene (C_2H_2) and propargyl (C_3H_3),^{14,15} as well as through several other growth mechanisms involving phenyl

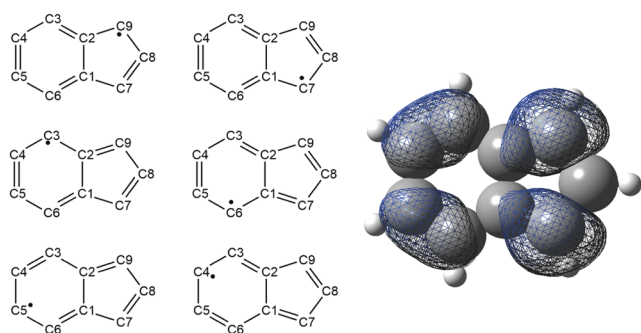
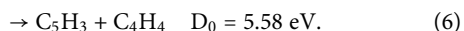
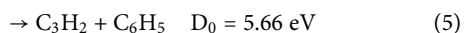
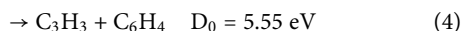
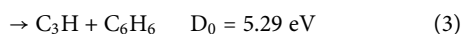
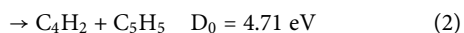
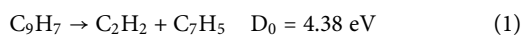


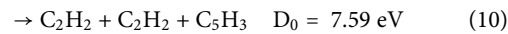
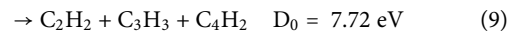
FIG. 1. Structure of the indenyl radical (C_9H_7). Left: Contributing resonance structures and carbon atom numbering scheme. Right: Alpha electron spin density determined at the M06-2X/6-31G(2df,p) level of theory, demonstrating delocalization across six resonance structures, with unpaired electron density predominantly located at C7/C9.

(C_6H_5), allene (C_3H_4), benzyl (C_7H_7), and propene (C_3H_6).^{16,17} In regard to the open-shell indenyl radical, theoretical investigations of the reactions between multiple C_2H_2 molecules and cyclopentadienyl (C_5H_5) have demonstrated the production of a cyclic C_9H_7 species with the radical center at C6, an isomer of the structures in Fig. 1.¹⁸ The reactions of fulvenallene (C_7H_6) and fulvenallenyl (C_7H_5) with small hydrocarbons have been implicated as participants in the production of two- and three-ringed PAHs,¹⁹ and C_9H_7 itself has been shown to associate with CH_3 to ultimately yield naphthalene ($C_{10}H_8$).²⁰ da Silva *et al.*²¹ examined the reaction of fulvenallene (C_7H_6) and C_2H_2 leading to the formation of C_9H_8 , which can lose a hydrogen atom to produce C_9H_7 . An extensive theoretical study examining the C_9H_7 potential energy surface was undertaken by Matsugi and Miyoshi,²² who determined the kinetics and mechanism of the benzyne (C_6H_4) + propargyl (C_3H_3) reaction. C_9H_7 participates as an intermediate species that can isomerize and then dissociate into acetylene and fulvenallenyl ($C_2H_2 + C_7H_5$). These theoretical studies suggest that $C_2H_2 + C_7H_5$ is a viable dissociation channel for C_9H_7 dissociation.

In this work, C_9H_7 photodissociation was investigated using fast beam photofragment translational spectroscopy at 248 nm and 193 nm. Equations (1)–(6) show the observable product channels at 193 nm (6.42 eV), not all of which are accessible at 248 nm (5.0 eV),^{21–26}



Additionally, there are multiple two- and three-body product channels [Eqs. (7)–(13)] that are energetically inaccessible for one photon absorption at 248 nm or 193 nm,^{5,6,21,22,26–30}



We definitively observe channel 1 at both 248 nm and 193 nm; this channel exhibits translational energy distributions that peak near zero but extend beyond the maximum available energy ($E_{T,MAX}$) for one-photon absorption, suggesting excess energy in the system. The three-body channels 9 and 10 are also observed, neither of which is one-photon accessible. It is thus proposed that multi-photon absorption by C_9H_7 occurs prior to dissociation, enabling these higher energy channels. In fact, analysis of the dissociation rates using Rice-Ramsperger-Kassel-Marcus (RRKM) theory indicates that all observed channels originate from two-photon absorption. Translational energy and angular distributions are consistent with all dissociation channels resulting from internal conversion followed by dissociation on the ground electronic state. A cursory examination of the data suggests additional contributions from the two-body channels 2 and 4, but further consideration indicates that these features are largely due to artifacts of our coincidence detection scheme. However, a convincing argument can be made implicating initial channels 2 and 4 production, followed by secondary C_5H_5 and C_6H_4 dissociation, respectively, to yield channel 9 at 193 nm.

II. METHODS

A. Experimental

Experiments were carried out using the Fast Radical Beam Machine (FRBM), which has been described in detail elsewhere.^{31–33} In brief, $C_9H_7^-$ anions were generated by bubbling 30 psig argon through indene (Sigma Aldrich, >99%) and expanding the gas mixture into vacuum through an Amsterdam Piezovalve operating at 100 Hz^{34,35} and then through a DC discharge source that was stabilized with an electron gun. $C_9H_7^-$ anions were skimmed, accelerated to 8 keV, separated by a Bakker time-of-flight mass spectrometer,^{36,37} and subsequently photodetached by 532 nm light from a Nd:YAG laser (Litron LPY742-100) to produce neutral C_9H_7 radicals. Dissociation of the partially deuterated $C_9H_5D_2$ radical (deuterated at C7 and C9; see Fig. 1) was performed by generating $C_9H_5D_2^-$ anions from a $C_9H_5D_3$ precursor with two D atoms on either C7 or C9. $C_9H_5D_3$ was synthesized according to the procedure as described in Bergson³⁸ and was purified via chromatography on SiO_2 .³⁹

The radicals were characterized by anion photoelectron (PE) spectroscopy using a velocity-map imaging spectrometer with its axis perpendicular to the ion beam.³³ The PE detector consisted of a chevron stack of MCPs coupled to a phosphor screen (Beam Imaging Solutions BOS-75) and CCD camera. PE spectra were generated by applying the BASEX algorithm⁴⁰ to acquired images to measure the PE kinetic energy distribution, thereby yielding an estimate of

the C_9H_7^- vibrational temperature and confirming the identity of the generated radicals.

Following photodetachment, any remaining anions in the beam were deflected, yielding a fast beam of neutral C_9H_7 radicals that were subsequently dissociated via 248 nm ($\sim 2\text{--}5$ mJ/pulse) or 193 nm light (~ 18 mJ/pulse) from a GAM EX-50 excimer laser. Dissociated fragments traveled 1.36 m (~ 12 μs), ultimately impinging on a Roentdek Hex80 Delay-Line Detector^{41,42} that collected position and time information for each fragment in coincidence, generating the fragment masses, translational energy release, and scattering angle for each two- and three-body dissociation event. The detector is gated such that only one dissociation event is detected within a 1 μs window, and two- and three-body events are distinguished by the number of events that hit the detector within that window. However, to minimize the possibility of false coincidences, in which particles are detected that do not originate from the same dissociating radical, the collection rate is kept to only a few events per second (on the order of 2–5).

A 2.9 mm radius beam block in front of the detector stopped undissociated C_9H_7 from hitting the detector. The presence of this beam block and the finite size of the detector prevented fragments with very high or low translational energy release from being detected. To compensate for this, the translational energy distributions incorporate a detector acceptance function (DAF).³²

The translational energy and angular distributions satisfy the following:

$$P(E_T, \theta) = P(E_T)[1 + \beta(E_T)P_2(\cos \theta)], \quad (14)$$

in which β is the translational energy-dependent anisotropy parameter and $P_2(\cos \theta)$ is the second Legendre polynomial.⁴³ The output of the GAM excimer laser is unpolarized, so θ is defined as the angle between the laser propagation direction and the recoil axis of dissociating fragments for two-body events or the normal to the plane of dissociation for three-body dissociation events, respectively. As a result, β ranges from -1 to $1/2$ for parallel and perpendicular processes, respectively, and is related to β_i , the anisotropy parameter that would be measured for linearly polarized light, by $\beta = -(1/2)\beta_i$.³³

B. Calculations

As will be discussed in Sec. III B, we observe features in the mass distributions preliminarily consistent with channels 1 ($\text{C}_2\text{H}_2 + \text{C}_7\text{H}_5$), 2 ($\text{C}_4\text{H}_2 + \text{C}_5\text{H}_5$), and 4 ($\text{C}_3\text{H}_3 + \text{C}_6\text{H}_4$). While a potential energy surface leading to the production of channels 1 and 4 has already been published,²² no information is available in the literature on the formation of channel 2. As such, calculations for all three channels were performed using the Gaussian 16 package⁴⁴ at the M06-2X/6-31G(2df,p) level of theory, with frequencies scaled by a factor of 0.9837.⁴⁵

The results of this theory are presented in Figs. S1–S3 of the [supplementary material](#) and were used for the subsequent rate constant calculations for two-body dissociation channels. The mean uncertainties associated with M06-2X level of theory and double zeta basis sets are ~ 1.5 kcal/mol.⁴⁶ Uncertainties of this magnitude are negligible in regard to the stationary points used for the rate

calculations. We saw no experimental evidence of channel 3 ($\text{C}_3\text{H} + \text{C}_6\text{H}_6$) and therefore did not include it in our calculations.

Rice-Ramsperger-Kassel-Marcus (RRKM) theory⁴⁷ was used to compute the rates of dissociation processes using the Mathematica program. In RRKM theory, the unimolecular rate constant is given by

$$k(E) = \frac{W^\ddagger(E - E_0)}{h\rho(E)}, \quad (15)$$

where h is Planck's constant, $\rho(E)$ is the rovibrational density of states of the reactants, and $W^\ddagger(E - E_0)$ is the sum of states of the transition states, both of which are calculated using the Beyer-Swinehart algorithm.⁴⁸

Rate constants were also calculated for secondary dissociation of C_7H_5 , C_5H_5 , and C_6H_4 . The dissociation pathways, geometries, and stationary points were acquired from da Silva *et al.*,^{29,49} and Ghigo *et al.*⁵⁰ for C_7H_5 , C_5H_5 , and C_6H_4 , respectively. The RRKM rates were calculated directly from the vibrational frequencies and energies taken from these sources at different levels of theory, making various assumptions of the energy content of these species.

III. RESULTS AND ANALYSIS

A. Anion photoelectron spectroscopy

The photoelectron spectrum of C_9H_7^- acquired at a photodetachment wavelength of 532 nm is presented in Fig. 2. The experimental spectrum is shown in black, and the red trace is a Franck-Condon simulation. The simulation was performed using ezSpectrum⁵⁰ with an assumed vibrational temperature of 300 K. Input C_9H_7^- and C_9H_7 vibrational frequencies were calculated using density functional theory at the B3LYP/6-311+G(d,p) level of theory in the Gaussian 09 package.⁵¹ Frequencies were scaled

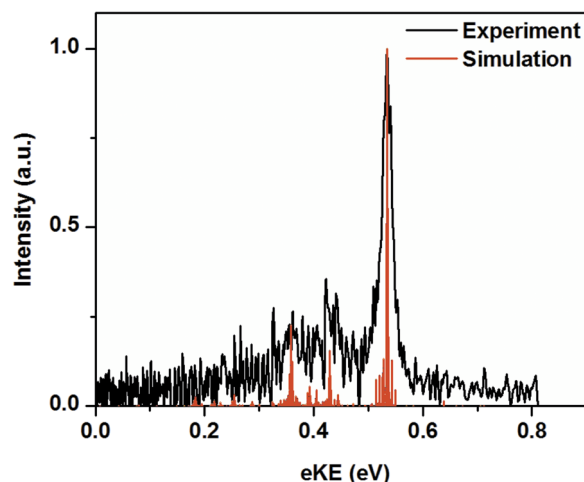


FIG. 2. Anion photoelectron spectrum of C_9H_7^- using 532 nm detachment wavelength, in which electron kinetic energy (eKE) is plotted against intensity. The black trace shows the experimental data, and the red trace presents a Franck-Condon simulation done at 300 K.

by 0.9679 according to the recommendation for Pople-style basis sets.⁵²

The most prominent feature in Fig. 2 corresponds to the vibrational origin transition yielding an electron affinity of 1.80 ± 0.02 eV, consistent with that found in previous work by Kim *et al.*¹¹ and which is clearly due to the indenyl radical. At lower electron kinetic energies, there are several weak features from vibrational excitation, but it is evident that most of the radicals produced are in their ground vibrational state with no obvious contribution from hot anions. Therefore, we approximate the internal energy of the radicals created by photodetachment at 532 nm, $E_{\text{INT,R}}$, to be 0 eV.

B. Photofragment mass distributions

Figure 3 presents the two-body [panels (a) and (b)] and three-body [panels (c) and (d)] mass distributions for the dissociation of C_9H_7 following excitation at 248 nm and 193 nm. At first glance in Fig. 3(a), there are three pairs of features centered around 39 and 76 Da, 26 and 89 Da, and 50 and 65 Da. The most prominent of these occurs at 39 and 76 Da and is consistent with dissociation channel 4, C_3H_3 and C_6H_4 . However, this channel is not energetically accessible from one photon absorption at 248 nm. There are

two additional pairs of peaks at 26 and 89 Da and 50 and 65 Da that match the masses for channel 1 ($\text{C}_2\text{H}_2 + \text{C}_7\text{H}_5$) and channel 2 ($\text{C}_4\text{H}_2 + \text{C}_5\text{H}_5$), respectively. Figure 3(b) shows the experimental two-body mass distribution from dissociation at 193 nm. It is similar to the two-body mass distribution at 248 nm in that there are again three sets of peaks that preliminarily correspond to the formation of channels 1, 2, and 4. Unlike 248 nm photodissociation, however, all three channels are energetically possible following the absorption of one photon of 193 nm.

Figures 3(c) and 3(d) present the three-body mass distributions for the dissociation of C_9H_7 at 248 nm and 193 nm, respectively. The largest features in panels (c) and (d) are the peaks at 26 Da. Each is accompanied by two peaks of similar intensity near 39 and 50 Da and a smaller shoulder near 63 Da. The peak at 26 Da is assigned to C_2H_2 , while 39, 50, and 63 Da are consistent with C_3H_3 , C_4H_2 , and C_5H_3 , respectively. As the peaks at 39 and 50 Da are of equal intensity, they are most likely from the same dissociation channel (channel 9), the remaining fragment of which must be C_2H_2 . Given that the 26 Da feature is considerably more intense than the peaks at 39 and 50 Da, C_2H_2 must also be produced in an additional channel; the most reasonable candidate is $\text{C}_2\text{H}_2 + \text{C}_2\text{H}_2 + \text{C}_5\text{H}_3$ (channel 10), which would account for the peak at 63 Da. The observation of channels 9 and 10 is notable since both

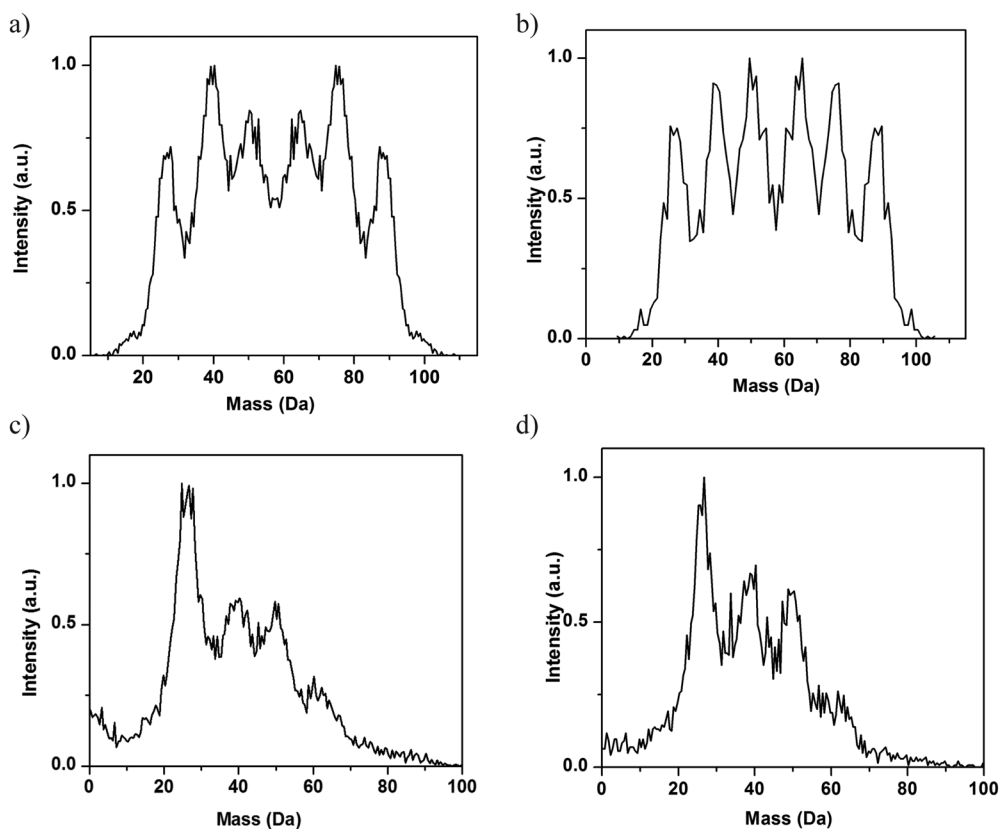


FIG. 3. Mass distributions of C_9H_7 dissociation. Panels (a) and (b) show the two-body distribution for dissociation using 248 nm and 193 nm, respectively. Panels (c) and (d) present the three-body distributions for dissociation using 248 nm and 193 nm, respectively.

channels (or indeed any three-body channels) require substantially more energy to form than is available from single photon absorption at 248 nm or 193 nm.

The mass resolution of our experiment is $m/\Delta m \approx 10$ such that mass channels separated by only 1 Da cannot be sufficiently distinguished.³¹ One method for understanding contributions from closely spaced channels is to simulate the mass distribution using the experimental translational energy distribution of the corresponding product channels.³³ Fitted simulations assuming the formation of channels 1, 2, and 4 are presented in Figs. S4 and S5 in the [supplementary material](#). These simulations rule out the formation of channel 5 ($C_3H_2 + C_6H_5$) and channel 8 ($C_4H_4 + C_5H_3$) for both wavelengths.

Additional insight into the product channels can come from dissociating the partially deuterated radical $C_9H_5D_2$, which has deuterium atoms on C7 and C9 (Fig. 1). Figure 4 presents the experimental two-body (a) and three-body (b) mass distributions for the dissociation of $C_9H_5D_2$ following absorption of a 193 nm photon (in red); the original C_9H_7 dissociation results are shown in black. Analogous experiments were not performed at 248 nm. Based on the dissociation pathways inferred from the potential energy surfaces shown in Figs. S1–S3, a single product fragment contains both deuterium atoms for each of the two-body dissociation pathways (fragment C_7H_5 , C_5H_5 , or C_3H_3 for channels 1, 2, or 4, respectively). Therefore, for each two-body channel, one of the peaks should shift by 2 Da.

The features corresponding to channel 1 at 26 and 89 Da [black trace in Fig. 4(a)] can be seen at 26 and 91 Da in the red trace, indicating that the deuterium atoms are located on the fulvenallenyl radical as is predicted from Fig. S1. However, shifts due to the deuterium atoms are considerably less obvious in the other sets of peaks. The feature at 65 Da corresponding to C_5H_5 of channel 2 does not appear to shift at all. Similarly, no shift in mass is evident in the C_3H_3 peak of channel 4 (39 and 76 Da). However, in the three-body experimental distribution shown in Fig. 4(b), the peak centered about 39 Da does shift so we would expect to see a similarly noticeable change in the 39 Da feature of the two-body distribution [Fig. 4(a)] were we truly detecting C_3HD_2 .

This set of observations suggests that the apparent presence of channels 2 and 4 may not be entirely due to true two-body

dissociation, specifically at 193 nm. One possible explanation for the observation of these features is that they result from the detection of false coincidence events from three-body dissociation and their misassignment to two-body events. In this instance, “false coincidence” refers to a three-body dissociation event in which only two of the three fragments hit the detector. Should the center of mass of these two fragments fall within the undissociated neutral beam center, then these events are accepted as two-body dissociation processes, and the fragment masses are dependent on the mass ratio of the two fragments that are detected. For example, a three-body event in which only C_4H_2 and C_3H_3 of channel 9 are detected would result in the same mass ratio as C_5H_5 and C_4H_2 and be classified as a valid coincidence event, assuming the center of mass of the collected particles can fall within the neutral beam center. Similarly, the mass ratio of C_6H_4 to C_3H_3 (channel 4) is the same as that of C_4H_2 to C_2H_2 (channel 9). Simulations of these false coincidences are shown in the [supplementary material](#) (Fig. S6).

In the formation of three-body products, such as C_2H_2 , C_3H_3 , and C_4H_2 of channel 9, the C_3H_3 radical is either singly deuterated if three-body dissociation proceeds through channels 1 or 2 or doubly deuterated if dissociation occurs through channel 4. In Sec. IV A, we will discuss the probability that channel 9 formation results from secondary dissociation of channels 1, 2, and 4. Therefore, the mass ratio for the two fragments detected out of three will not likely change substantially because many of these fragments (C_2H_2 , C_3H_3 , or C_4H_2) will be singly deuterated or nondeuterated. For false two-body events such as these, we would not expect to observe a clearly defined shift in the two-body mass distribution, as is the case in Fig. 4(a) for the features corresponding to channels 2 and 4. We do, however, observe a distinct shift in the peak at 39 Da in the three-body distribution in Fig. 4(b), which implies the detection of either C_3H_2D or C_3HD_2 . Hence, although we are not confident in our observation of channels 2 or 4 in the two-body distribution, the deuterated results suggest that some channel 9 yield originates from a mechanism that involves the initial formation of these channels, at least at 193 nm.

While we apparently observe features consistent with channels 2 and 4, we cannot claim to know to what extent any true two-body dissociation is observed. At 193 nm, the deuterated results provide a convincing argument that the features from these

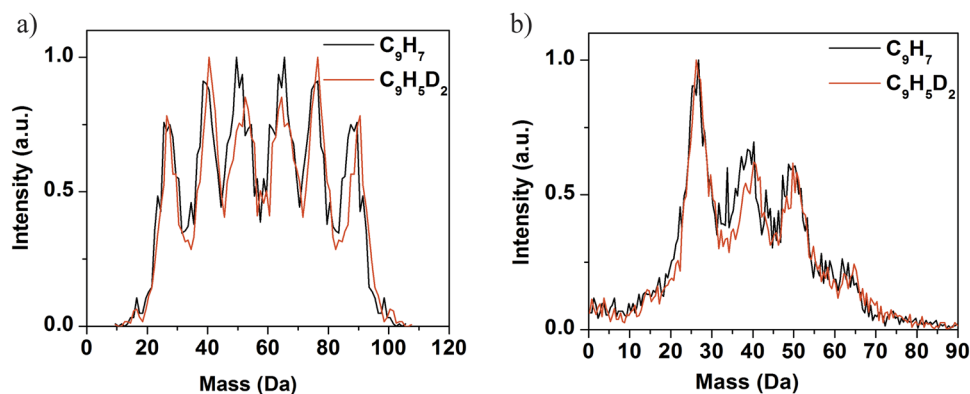


FIG. 4. Two-body (a) and three-body (b) mass distributions of the dissociation of $C_9H_5D_2$ (red) vs C_9H_7 (black) at 193 nm.

channels are largely due to false coincidences, while at 248 nm, we do not have sufficient data to say. Thus, the only two-body channel of reasonable confidence is channel 1, and as such, it will be the sole two-body channel analyzed in Sec. III C.

C. Translational energy distributions

For each dissociation event, the translational energy of the observed products is given by

$$E_T = h\nu - D_0 + E_{\text{INT,R}} - E_{\text{INT,P}}, \quad (16)$$

where $h\nu$ is the photon energy, D_0 is the energy required for dissociation, $E_{\text{INT,R}}$ is the internal energy of the C_9H_7 radicals prior to dissociation, and $E_{\text{INT,P}}$ is the internal energy of the products. As discussed in Sec. III A, most of the indenyl radicals are produced in their ground vibrational state, so $E_{\text{INT,R}}$ is assumed to be zero.

Figure 5 presents the translational energy distribution for channel 1 ($\text{C}_2\text{H}_2 + \text{C}_7\text{H}_5$). The blue and red traces correspond to the distributions for dissociation from excitation at 248 nm and 193 nm, respectively, and correspondingly colored arrows mark the maximum available energy ($E_{\text{T,MAX}}$) for one-photon dissociation at each wavelength. The distributions peak just below 0.5 eV, and the associated angular distributions are isotropic, indicating that the excited C_9H_7 radical persists longer than a rotational period before dissociating. Notably, at 248 nm, the distribution extends well beyond $E_{\text{T,MAX}}$, while at 193 nm, the distribution extends up to $E_{\text{T,MAX}}$. In combination with energetically inaccessible three-body dissociation channels and RRKM calculations described in Sec. III D, these results suggest that dissociation occurs following the absorption of two photons. This notion is supported by a power study we performed which shows a quadratic dependence of raw coincident events observed on the laser power at both 248 nm and

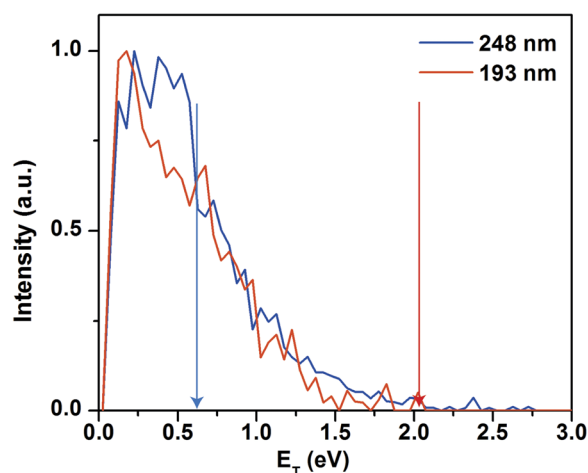


FIG. 5. Translational energy distributions for C_9H_7 dissociation into channel 1 ($\text{C}_2\text{H}_2 + \text{C}_7\text{H}_5$). The blue and red traces correspond to dissociation using 248 nm and 193 nm, respectively. The blue and red arrows correspond to $E_{\text{T,MAX}}$ for single photon processes at 248 nm and 193 nm, respectively.

193 nm; this is presented in the [supplementary material](#) (Fig. S7). Typical rates for internal conversion processes are on the order of $\sim 10^{-12}$ s,⁵³ and our dissociation laser pulse is ~ 16 ns. Therefore, it is plausible that following absorption of the first photon, C_9H_7 internally converts to its ground electronic state before absorbing a second photon. The underlying requirement that the dissociation lifetime is much longer than 16 ns is supported by the calculations in Sec. III D.

Figures 6(a) and 6(b) show the translational energy releases for the three-body channels 9 ($\text{C}_2\text{H}_2 + \text{C}_3\text{H}_3 + \text{C}_4\text{H}_2$) and 10 ($\text{C}_2\text{H}_2 + \text{C}_2\text{H}_2 + \text{C}_5\text{H}_3$), respectively. As neither of these dissociation channels is energetically accessible following one-photon absorption at the energies used, the maximum available energy for a two-photon process ($E_{\text{T,MAX,2}}$) is marked in blue for 248 nm, while the maximum

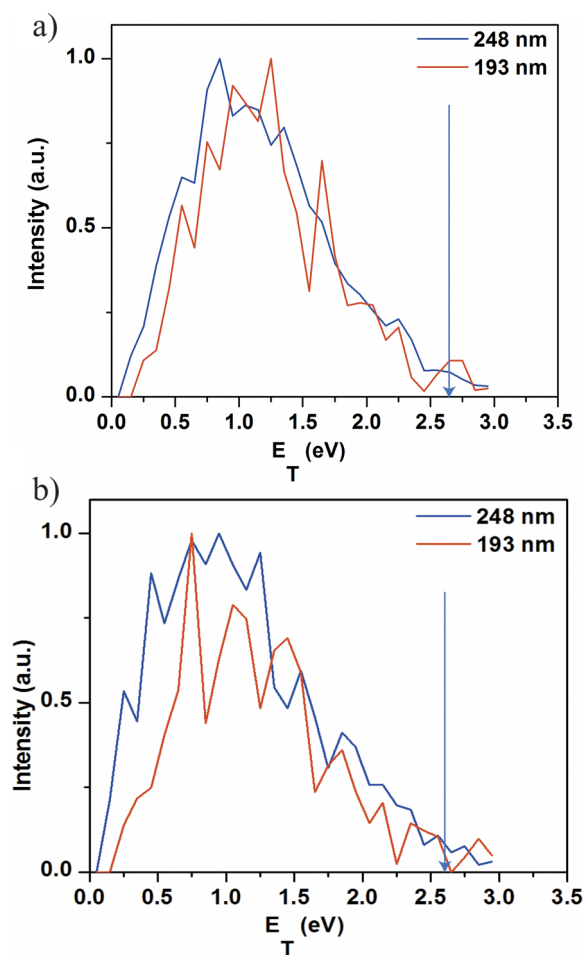


FIG. 6. Three-body translational energy distributions for dissociation to channel 9 ($\text{C}_2\text{H}_2 + \text{C}_3\text{H}_3 + \text{C}_4\text{H}_2$) (a) and channel 10 ($\text{C}_2\text{H}_2 + \text{C}_2\text{H}_2 + \text{C}_5\text{H}_3$) (b). The blue and red traces correspond to dissociation using 248 nm and 193 nm, respectively. The blue arrow in each distribution corresponds to the maximum available energy for dissociation via two photons of 248 nm ($E_{\text{T,MAX,2}}$). $E_{\text{T,MAX,2}}$ for dissociation from two photons of 193 nm is not marked as it lies beyond the x-axis scale.

available energy for two-photon absorption of 193 nm is beyond the scale of the x-axes and is not marked.

For both channels, these distributions are broad and tail off near $E_{T,MAX,2}$ for 248 nm. For channel 9, $\beta = -0.20 \pm 0.04$ and $\beta = -0.24 \pm 0.06$ for 248 nm and 193 nm, respectively. Similarly, for channel 10, $\beta = -0.21 \pm 0.07$ and $\beta = -0.07 \pm 0.12$ for 248 nm and 193 nm, respectively. In our experiment, a negative value of β for three-body dissociation would indicate the propensity of dissociation plane to lie perpendicular to the laser polarization plane, and the somewhat negative values of β are suggestive that this is the case for channels 9 and 10. This result is of concern given that the two-body dissociation to channel 1 is isotropic. However, the three-body angular distributions are not DAF-corrected, which may account for the slight anisotropy observed.

To examine the angular results further, simulations were performed assuming the three-body products are formed sequentially (i.e., dissociation of C_9H_7 into $C_2H_2 + C_7H_5$, followed by C_7H_5 fragmentation after some time) through two steps, each of which involves a translational energy release associated with isotropic angular distributions. For the first step, $C_9H_7 \rightarrow C_2H_2 + C_7H_5$, the translational energy distribution of channel 1 was used for the simulation. The second release step was simulated via multiple methods that are described and compared in the [supplementary material](#). The simulated arrival times and positions were analyzed in the same manner as the raw experimental data, and the associated anisotropy parameters are shown in Table S1. They are nonzero and negative, like the experimental results, despite the simulations assuming isotropic angular distributions. As such, we suspect that we are not uniformly detecting fragments over all scattering angles and that the three-body results are in fact consistent with an isotropic angular distribution.

Three-body dissociation events can often be investigated further using Dalitz plots⁵⁴ in which the fraction of translational energy imparted to each fragment is plotted for all three fragments, thus providing a sense of the relative amounts of translational energy in each product. The Dalitz plots for channels 9 and 10 depict relatively uniform distributions and will not be discussed in detail here but are included in the [supplementary material](#) for completeness (Fig. S11).

For the three product channels conclusively observed, channels 1, 9, and 10, the translational energy distributions in Figs. 5 and 6 peak well below $E_{T,MAX,2}$ for experiments performed at both dissociation energies, are associated with isotropic angular distributions, and are similar regardless of the dissociation energy used. For a two-photon process, which we argue is necessary for all observed dissociation, excited state products are energetically accessible, but dissociation on an excited electronic state would typically be characterized by distinguishable translational energy distributions for each dissociation wavelength, in addition to an anisotropic angular distribution. As such, we conclude that dissociation proceeds on the ground electronic state for all three channels, and our further analysis assumes this is the case.

D. RRKM calculations

For ground state processes, it is appropriate to use RRKM theory (Sec. II B) to gain additional insight into the dissociation

mechanisms. Table I presents the RRKM rates for the dissociation of C_9H_7 to channels 1, 2, and 4 following one- and two-photon absorption. We include channels 2 and 4 in these calculations to further our understanding of the extent to which these channels are from detection artifacts.

According to the work by Matsugi and co-workers²² and the surfaces shown in Figs. S1–S3, production of channels 1, 2, and 4 all require traversing barriers that lie more than 5.0 eV above C_9H_7 , so they should not be produced from one photon of 248 nm. The formation of channels 1, 2, and 4 from 193 nm is energetically possible, but our calculations indicate that dissociation occurs too slowly to be observed in our experiment. The transit time for the radicals from the dissociation laser interaction region to the detector is $\sim 12 \mu s$, so the minimum rate constant of dissociation necessary for the detection is on the order of $10^5 s^{-1}$.

These slow rates support the notion that our dissociation results do not stem from a one-photon process, thereby suggesting that the C_9H_7 radical absorbs two photons prior to any dissociation. In the right columns of the table, the rate constants of C_9H_7 dissociation following the absorption of two photons of either 248 nm or 193 nm are shown. All three channels have sufficiently fast rate constants such that the two-body photofragments should be detectable if secondary fragmentation of the products does not occur.

We can also use the RRKM results to explore the production of the three-body channels. For two-photon absorption, C_7H_5 , C_5H_5 , and C_6H_4 can be produced with enough energy to further fragment. This would lead to channel 9 in each case, and previous experiments have shown that the secondary dissociation of C_7H_5 of channel 1 can also lead ultimately to channel 10 ($C_2H_2 + C_2H_2 + C_5H_3$).⁵⁵ Table II presents the results of these secondary dissociation RRKM results, assuming that all available energy is available to the dissociating fragment, with no energy going into translation or the other cofragment.

The results presented in Table II indicate that sequential three-body dissociation to channels 9 and 10 can occur well within the detection time window of our experiment, thus providing a possible explanation for why we observe contamination of the two-body mass distribution by false coincident events. However, under the assumptions of energy disposal used to generate Table II, the secondary dissociation rates are upper bounds, as discussed further in Sec. IV A.

E. Branching ratios

Estimated experimental branching ratios are presented in Table III based on the assumption that channel 1 is the only

TABLE I. RRKM results of C_9H_7 dissociation.

Channel	Rate (s^{-1})			
	248 nm (5.00 eV)	193 nm (6.42 eV)	248 nm \times 2 (10.00 eV)	193 nm \times 2 (12.84 eV)
1 ($C_2H_2 + C_7H_5$)	N/A	1.5×10^2	4.1×10^7	2.7×10^9
2 ($C_4H_2 + C_5H_5$)	N/A	3.8×10^2	1.8×10^8	7.9×10^9
4 ($C_3H_3 + C_6H_4$)	N/A	1.6	6.7×10^7	8.8×10^9

TABLE II. RRKM results of secondary dissociation processes.

Secondary dissociation pathway	Rate (s^{-1})	
	248 nm \times 2 (10.0 eV)	193 nm \times 2 (12.84 eV)
$\text{C}_2\text{H}_2 + \text{C}_7\text{H}_5 \rightarrow \text{C}_2\text{H}_2 + \text{C}_3\text{H}_3 + \text{C}_4\text{H}_2$ (channel 9)	1.7×10^7	3.5×10^9
$\text{C}_2\text{H}_2 + \text{C}_7\text{H}_5 \rightarrow \text{C}_2\text{H}_2 + \text{C}_2\text{H}_2 + \text{C}_5\text{H}_3$ (channel 10)	3.8×10^6	8.0×10^9
$\text{C}_4\text{H}_2 + \text{C}_5\text{H}_5 \rightarrow \text{C}_2\text{H}_2 + \text{C}_3\text{H}_3 + \text{C}_4\text{H}_2$ (channel 9)	2.0×10^8	1.5×10^{10}
$\text{C}_3\text{H}_3 + \text{C}_6\text{H}_4 \rightarrow \text{C}_2\text{H}_2 + \text{C}_3\text{H}_3 + \text{C}_4\text{H}_2$ (channel 9)	1.7×10^3	3.4×10^8

TABLE III. Experimental branching ratios.

	Percentage of total events		
	1 ($\text{C}_2\text{H}_2 + \text{C}_7\text{H}_5$)	9 ($\text{C}_2\text{H}_2 + \text{C}_3\text{H}_3 + \text{C}_4\text{H}_2$)	10 ($\text{C}_2\text{H}_2 + \text{C}_2\text{H}_2 + \text{C}_5\text{H}_3$)
248 nm	36 ± 12	43 ± 8	21 ± 4
193 nm	23 ± 3	57 ± 3	20 ± 1

two-body channel, as we cannot confirm or eliminate channels 2 or 4. Raw experimental counts were used to determine the branching ratios of each channel. However, the Roentdek detector has a one-particle detection efficiency of $p = 0.6$.⁵⁶ Therefore, the likelihood of detecting a two-body event is $p_{\text{two-body}} = 0.36$ and a three-body event is $p_{\text{three-body}} = 0.22$.⁵⁶ The two- and three-body channels have been corrected for these differences in detection efficiency, and the results are presented in Table III. The reported error bars are associated with the standard deviation of the branching ratios across all data sets at a given dissociation wavelength (i.e., they are random errors).

It should be mentioned that the one-particle detection efficiency is valid only for events that impinge on the detector. The correction applied to the three-body channels does not account for three-body events in which only two of three fragments are detected if the third fragment does not hit the detector. As discussed in Sec. III B, the features consistent with channels 2 and 4 are, at least in part, attributed to these types of false coincidence events. Therefore, the branching ratios presented in Table III for channels 9 and 10 are lower bounds for the true number of three-body events.

IV. DISCUSSION

A. Two-body dissociation

For both 248 nm and 193 nm, channel 1 ($\text{C}_2\text{H}_2 + \text{C}_7\text{H}_5$) is the only confirmed two-body product channel. The low-peaking translational energy distributions and the independence of the distributions regardless of the dissociation energy used suggest that dissociation occurs on the ground electronic state, as discussed in Sec. III C. Dissociation on the ground electronic state implies that the two-body channel with the fastest RRKM rate constant should be the dominant channel. According to Table I, this is channel 2 ($\text{C}_4\text{H}_2 + \text{C}_5\text{H}_5$), not channel 1. However, the rates for secondary dissociation processes presented in Table II indicate that the rate of

dissociation of C_5H_5 to ultimately yield channel 9 ($\text{C}_2\text{H}_2 + \text{C}_3\text{H}_3 + \text{C}_4\text{H}_2$) is >10 times the rate of C_7H_5 fragmentation at 248 nm, assuming both radicals have access to all the available energy following the primary dissociation step. While it is unlikely that the radicals actually do have access to all the available energy (cofragments C_2H_2 and C_4H_2 may have some internal energy), the rates in Table II are a strong indication that any $\text{C}_4\text{H}_2 + \text{C}_5\text{H}_5$ formed in the primary step undergoes secondary dissociation through which the C_5H_5 fragment falls apart to C_2H_2 and C_3H_3 , as it has been shown to do.⁶

Despite the prediction that C_7H_5 falls apart more slowly than C_5H_5 , the rate constants in Table II show that C_7H_5 can undergo reasonably rapid secondary dissociation. Under these circumstances, it is surprising that so much two-body dissociation to channel 1 is observed. This issue is addressed in Fig. 7 in which the rates of the secondary dissociation for C_7H_5 (green), C_5H_5 (blue), and C_6H_4 (red) into channel 9 are plotted vs the energy available to that fragment after the primary dissociation step from C_9H_7 for a two-photon process [Fig. 4(b)]. The rate for C_7H_5 to fall apart into channel 10 ($\text{C}_2\text{H}_2 + \text{C}_2\text{H}_2 + \text{C}_5\text{H}_3$) is shown in orange in Fig. 7. The gray line marks the limiting rate (10^5 s^{-1}), slower than which dissociation cannot be detected in our experiment. Figure 4(a) presents a diagram describing the available energy quantities used in Fig. 4(b).

The blue curve, corresponding to C_5H_5 secondary dissociation, is clearly the fastest. If one assumes that C_7H_5 has access to all the available energy at each dissociation wavelength (5.62 eV and 8.46 eV for two photons of 248 nm and 193 nm, respectively, as assumed in Table II), then it clearly has enough energy to fragment further. However, when accounting for translational energy and possible internal energy in the cofragment, we see why C_7H_5 does not always fall apart. The translational energy distribution for channel 1 in Fig. 5 indicates that $\text{C}_2\text{H}_2 + \text{C}_7\text{H}_5$ fragments recoil with up to 1.5 eV of translational energy. As such, for experiments performed at 248 nm, C_7H_5 would not likely

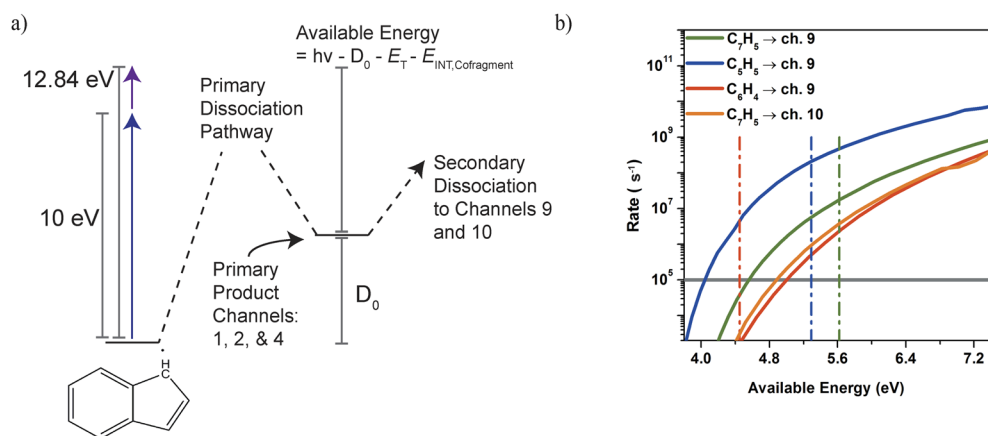


FIG. 7. Panel (a) presents a diagram to describe the value of the available energy used in panel (b) (i.e., the remaining energy after the primary product channel is formed). Panel (b) shows a plot of the RRKM rate constants for secondary dissociation of C_7H_5 (green), C_5H_5 (blue), and C_6H_4 (red) to channel 9 and C_7H_5 to channel 10 (orange), are shown as a function of available energy. The dotted vertical lines mark the maximum available energy for secondary dissociation for experiments performed at 248 nm, with each color corresponding to each corresponding fragment. The green vertical line marks the maximum available energy for secondary C_7H_5 dissociation. The gray line marks the limiting rate (10^5 s^{-1}), slower than which dissociation cannot be detected in our experiment.

dissociate further, as this decrease in the available energy substantially reduces its dissociation rate (i.e., below the gray line). Any internal energy imparted to the acetylene fragment would further detract from the available energy of C_7H_5 such that it remains intact.

In moving to 193 nm, Table II implies that most, if not all, of C_7H_5 should fall apart further to channels 9 and 10 given the available energy for two photons of this wavelength. While it is true that the branching ratio of channel 1 decreases in moving to 193 nm, it still accounts for 23% of the total product yield. Thus, we are led to conclude that internal energy in the cofragment accounts for evidence of channel 1 at 193 nm.

The same analysis can be performed for channel 4 ($C_3H_3 + C_6H_4$) and subsequent C_6H_4 dissociation. We have already indicated that features consistent with channel 4 in the two-body mass distributions are, at least in part, due to detection artifacts, such that we do not know if there is any true channel 4 production. For ground state dissociation at 248 nm, the channel 4 RRKM rate constant is faster than that of channel 1 according to Table I, and secondary dissociation of C_6H_4 is slow, meaning that three-body dissociation through this pathway is unlikely. As such, one would expect that channel 4 should be observed at 248 nm. Part of our uncertainty about channel 4 production stems from the lack of a distinguishable shift in mass for the peak at 39 Da [Fig. 4(a)] in the dissociation of $C_9H_5D_2$. Note, however, that these dissociation data were only collected at 193 nm, not at 248 nm. Therefore, we cannot eliminate the possibility that the $C_9H_5D_2$ results would demonstrate clear evidence of at least some true channel 4 at 248 nm. Moreover, in moving to 193 nm, we see a considerable increase in the rate constant for C_6H_4 secondary dissociation and an associated increase in the channel 9 branching ratio. This could, in fact, be evidence for true channel 4 production, but at 193 nm, the C_6H_4 fragment consistently falls apart further into $C_2H_2 + C_4H_2$. Therefore, we do not observe obvious evidence of channel 4 in the dissociation of $C_9H_5D_2$ at 193 nm.

B. Three-body dissociation

The translational energy distributions for dissociation to channels 9 ($C_2H_2 + C_3H_3 + C_4H_2$) and 10 ($C_2H_2 + C_2H_2 + C_5H_3$) are presented in Fig. 6, and as was discussed at the end of Sec. III C, it is consistent with a ground state dissociation mechanism. Therefore, we limit our discussion in this section to the branching ratios and time scales of the three-body mechanisms.

We claimed in Sec. IV A that channel 9 is formed through the secondary dissociation of both C_7H_5 and C_5H_5 , the latter more readily than the former, and C_6H_4 , for experiments performed at 193 nm. We further support this claim by examining Fig. 4(b), which shows the three-body mass distribution for $C_9H_5D_2$ dissociation at 193 nm. Invoking the ground state pathways available in the literature for C_7H_5 and C_5H_5 , we find that should channel 9 proceed through C_7H_5 , the resultant deuterated products are $C_2H_2 + C_3H_2D + C_4HD$,²⁹ whereas they are $C_2HD + C_3H_2D + C_4H_2$ if dissociation occurs through C_5H_5 .⁴⁹ Regardless of the mechanism, the propargyl radical becomes deuterated, as is evident in the noticeable shift in the 39 Da feature in Fig. 4(b). The other features do not noticeably shift as they are only sometimes deuterated, which is consistent with the evidence that channel 9 can proceed through either channel 1 or channel 2. With respect to secondary dissociation of C_6H_4 , the expected deuterated product channel would be $C_2H_2 + C_3HD_2 + C_4H_2$, which is again consistent with the observed mass distribution in Fig. 4(b). Therefore, channel 4 may also be a viable pathway through which channel 9 is produced.

As we have concluded that C_7H_5 from channel 1 fragments further into channels 9 and 10, the branching ratio of channel 9:channel 10 should be somewhat similar to that of secondary C_7H_5 dissociation into $C_3H_3 + C_4H_2$ and $C_2H_2 + C_5H_3$ (although secondary dissociation of C_5H_5 and possibly C_6H_4 should also contribute to channel 9 yield in our work). Ramphal *et al.*⁵⁵ cited 5.6:1 and 4:1 ratios for $C_3H_3:C_2H_2$ formation at 248 nm and 193 nm, respectively. Earlier work examining the pyrolysis of C_7H_6 and

C_7H_5 also saw significantly more $C_3H_3 + C_4H_2$ than $C_2H_2 + C_5H_3$, although additional reactions in the pyrolysis source did not allow for clear quantification of this ratio.⁵⁷ While our branching ratios for channel 9 to channel 10 include a large number of assumptions that complicate a detailed comparison, we do find channel 9 to be the dominant three-body channel, which is at least consistent with previous results. Interestingly, the channel 10 yield does not appear to change substantially in moving to 193 nm, although the calculated rates increase dramatically with increasing available energy. However, at 193 nm, there are three possible mechanisms through which channel 9 can be formed (i.e., through secondary dissociation of C_7H_5 , C_5H_5 , and C_6H_4) such that ultimately the combined rate to produce channel 9 is significantly greater than that to yield channel 10. As such, while channel 10 is likely generated in a higher yield at 193 nm, this change is compensated by the significant yield of channel 9.

Finally, we consider the time scales on which channels 9 and 10 are formed. Three-body dissociation events are classified as concerted, asynchronous concerted, or sequential.⁵⁸ Concerted events result in the production of all three fragments simultaneously, whereas asynchronous concerted and sequential events result in some time passing between the first and second dissociation, either faster or slower than a rotational period, respectively.⁵⁸ Typically, Dalitz plots are used to understand these time scales; however, the Dalitz plots (Fig. S11) for channels 9 and 10 show a uniform distribution across the entire plot.

Given the ground state nature of the dissociation to channels 9 and 10, a sequential mechanism may be expected, in which $C_2H_2 + C_7H_5$ is formed, followed by fragmentation of C_7H_5 . Alternatively, we have already discussed that C_5H_5 , formed as a fragment of channel 2, should readily dissociate into $C_2H_2 + C_3H_3$, ultimately yielding channel 9. The RRKM rate constants in Table II for secondary dissociation of C_7H_5 and C_5H_5 at 248 nm are generally slow compared with the general range of rotational motion for larger molecules (10^{-10} – 10^{-11} s),⁵³ thereby implying that the fragments are intact while rotating and dissociation occurs in a more sequential manner. In moving to 193 nm, the conclusions are similar with the added possibility of C_6H_4 fragmentation to yield channel 9.

V. CONCLUSION

Photodissociation wavelengths of 248 nm and 193 nm were used to dissociate C_9H_7 , and two- and three-body dissociation products were detected in coincidence. C_9H_7 was found to dissociate following the absorption of two photons and dissociate into $C_2H_2 + C_7H_5$, $C_2H_2 + C_3H_3 + C_4H_2$, and $C_2H_2 + C_2H_2 + C_5H_3$. All dissociation was determined to occur via ground state dissociation processes following internal conversion to the ground electronic state. The formation of $C_2H_2 + C_3H_3 + C_4H_2$ can occur through further dissociation of C_7H_5 and C_5H_5 at 248 nm as well as C_6H_4 dissociation at 193 nm. $C_2H_2 + C_2H_2 + C_5H_3$ likely originates exclusively from further fragmentation of C_7H_5 .

Features attributed to $C_4H_2 + C_5H_5$ and $C_3H_3 + C_6H_4$ were also observed, but ultimately, we remain unclear about the extent to which these two-body products were formed without falling apart further. It is evident, however, that both experimental results and RRKM calculations demonstrate the propensity for the C_9H_7 radical to remain intact, which is a notable finding given the collective

interest in PAH reactivity. The large quantity of energy required to dissociate this radical is evidence that it may participate favorably in PAH growth mechanisms and thus may be a worthwhile system to model general PAH aggregation.

The unimolecular dissociation of the C_9H_7 is a complex problem yielding a wealth of experimental data, not all of which can be readily interpreted based on the work described herein. As this species is not well represented in the literature, this study has shown that more work via a variety of comprehensive experimental and theoretical techniques is necessary to truly understand the behavior of this benchmark PAH radical.

SUPPLEMENTARY MATERIAL

See the [supplementary material](#) for potential energy surfaces, simulations, power study results, Dalitz plots, and dissociation results at 225 nm and 157 nm.

ACKNOWLEDGMENTS

This research was supported by the Director, Office of Basic Energy Science, Chemical Sciences Division of the U.S. Department of Energy under Contract No. DE-AC02-05CH11231, the Australian Research Council Future Fellowship program under Grant No. FT130101340, and the National Institutes of Health under Grant No. S10OD023532. The authors would also like to thank Mark Shapero and Isaac Ramphal for access to previous results regarding C_7H_5 and C_5H_5 dissociation as well as for several fruitful discussions.

REFERENCES

- ¹J. L. Durant, W. F. Busby, Jr., A. L. Lafleur, B. W. Penman, and C. L. Crespi, *Mutat. Res./Genet. Toxicol.* **371**, 123 (1996).
- ²A. G. G. M. Tielens, *Rev. Mod. Phys.* **85**, 1021 (2013).
- ³H. Richter and J. B. Howard, *Prog. Energy Combust. Sci.* **26**, 565 (2000).
- ⁴S. Granata, T. Faravelli, E. Ranzi, N. Olten, and S. Senkan, *Combust. Flame* **131**, 273 (2002).
- ⁵T. L. Nguyen, T. N. Le, and A. M. Mebel, *J. Phys. Org. Chem.* **14**, 131 (2001).
- ⁶M. Shapero, I. A. Ramphal, and D. M. Neumark, *J. Phys. Chem. A* **122**, 4265 (2018).
- ⁷H. Richter, W. J. Greico, and J. B. Howard, *Combust. Flame* **119**, 1 (1999).
- ⁸V. V. Kislov and A. M. Mebel, *J. Phys. Chem. A* **111**, 3922 (2007).
- ⁹T. Izumida, K. Inoue, S. Noda, and H. Yoshida, *Bull. Chem. Soc. Jpn.* **54**, 2517 (1981).
- ¹⁰B. Römer, G. A. Janaway, and J. I. Brauman, *J. Am. Chem. Soc.* **119**, 2249 (1997).
- ¹¹J. B. Kim, M. L. Weichman, T. I. Yacovitch, C. Shih, and D. M. Neumark, *J. Chem. Phys.* **139**, 104301 (2013).
- ¹²P. Hemberger, M. Steinbauer, M. Schneider, I. Fischer, M. Johnson, A. Bodi, and T. Gerber, *J. Phys. Chem. A* **114**, 4698 (2010).
- ¹³R. F. Pottier and F. P. Lossing, *J. Am. Chem. Soc.* **85**, 269 (1963).
- ¹⁴V. D. Knyazev and I. R. Slagle, *J. Phys. Chem. A* **106**, 5613 (2002).
- ¹⁵J. D. Savee, T. M. Selby, O. Welz, C. A. Taatjes, and D. L. Osborn, *J. Phys. Chem. Lett.* **6**, 4153 (2015).
- ¹⁶A. M. Mebel, Y. Gerogievskii, A. W. Jasper, and S. J. Klippenstein, *Faraday Discuss.* **195**, 637 (2016).
- ¹⁷A. M. Mebel, A. Landera, and R. I. Kaiser, *J. Phys. Chem. A* **121**, 901 (2017).
- ¹⁸S. Fascella, C. Cavallotti, R. Rota, and S. Carra, *J. Phys. Chem. A* **109**, 7546 (2005).
- ¹⁹G. da Silva and J. W. Bozzelli, *J. Phys. Chem. A* **113**, 12045 (2009).
- ²⁰L. Zhao, R. I. Kaiser, W. Lu, B. Xu, M. Ahmed, A. N. Morozov, A. M. Mebel, A. H. Howlader, and S. F. Wnuk, *Nat. Commun.* **10**, 1510 (2019).

- ²¹G. da Silva and J. W. Bozzelli, *J. Phys. Chem. A* **113**, 8971 (2009).
- ²²A. Matsugi and A. Miyoshi, *Phys. Chem. Chem. Phys.* **14**, 9722 (2012).
- ²³J. A. Miller and C. F. Melius, *Combust. Flame* **91**, 21 (1992).
- ²⁴C. F. Melius, J. A. Miller, and E. M. Evleth, *Symp. (Int.) Combust.* **24**, 621 (1992).
- ²⁵L. V. Moskaleva and M. C. Lin, *J. Comput. Chem.* **21**, 415 (2000).
- ²⁶B. Ruscic and D. H. Bross, Active Thermochemical Tables (ATcT) values based on version 1.122 of the Thermochemical Network, available at ATcT.anl.gov, 2016.
- ²⁷S. J. Klippenstein and J. A. Miller, *J. Phys. Chem. A* **109**, 4285 (2005).
- ²⁸A. Jamal and A. M. Mebel, *Phys. Chem. Chem. Phys.* **12**, 2606 (2009).
- ²⁹G. da Silva and A. J. Trevitt, *Phys. Chem. Chem. Phys.* **13**, 8940 (2011).
- ³⁰G. Ghigo, A. Maranzana, and G. Tonachini, *Phys. Chem. Chem. Phys.* **16**, 23944 (2014).
- ³¹D. R. Cyr, D. J. Leahy, D. L. Osborn, R. E. Continetti, and D. M. Neumark, *J. Chem. Phys.* **99**, 8751 (1993).
- ³²D. L. Osborn, H. Choi, D. H. Mordaunt, R. T. Bise, D. M. Neumark, and C. M. Rohlfing, *J. Chem. Phys.* **106**, 3049 (1997).
- ³³A. W. Harrison, M. Ryazanov, E. N. Sullivan, and D. M. Neumark, *J. Chem. Phys.* **145**, 024305 (2016).
- ³⁴D. Irimia, R. Kortekaas, and M. H. M. Janssen, *Phys. Chem. Chem. Phys.* **11**, 3958 (2009).
- ³⁵D. Irimia, D. Dobrikov, R. Kortekaas, H. Voet, D. A. van den Ende, W. A. Groen, and M. H. M. Janssen, *Rev. Sci. Instrum.* **80**, 113303 (2009).
- ³⁶J. M. B. Bakker, *J. Phys. E: Sci. Instrum.* **6**, 785 (1973).
- ³⁷J. M. B. Bakker, *J. Phys. E: Sci. Instrum.* **7**, 364 (1974).
- ³⁸G. Bergson, *Acta Chem. Scand.* **18**, 2003 (1964).
- ³⁹C. Rav-Acha, E. Choshen (Goldstein), and S. Sarel, *Helv. Chim. Acta* **69**, 1728 (1984).
- ⁴⁰V. Dribinski, A. Ossadtchi, V. A. Mandelshtam, and H. Reisler, *Rev. Sci. Instrum.* **73**, 2634 (2002).
- ⁴¹O. Jagutzki, A. Cerezo, A. Czasch, R. Dörner, M. Hattas, M. Huang, V. Mergel, U. Spillmann, K. Ullmann-Pfleger, T. Weber, H. Schmidt-Böcking, and G. D. W. Smith, *IEEE Trans. Nucl. Sci.* **49**, 2477 (2002).
- ⁴²A. W. Harrison, J. S. Lim, M. Ryazanov, G. Wang, S. Gao, and D. M. Neumark, *J. Phys. Chem. A* **117**, 11970 (2013).
- ⁴³R. N. Zare, *Mol. Photochem.* **4**, 1 (1972).
- ⁴⁴M. J. Frisch, G. W. Trucks, H. B. Schlegel, G. E. Scuseria, M. A. Robb, J. R. Cheeseman, G. Scalmani, V. Barone, G. A. Petersson, H. Nakatsuji, X. Li, M. Caricato, A. V. Marenich, J. Bloino, B. G. Janesko, R. Gomperts, B. Mennucci, H. P. Hratchian, J. V. Ortiz, A. F. Izmaylov, J. L. Sonnenberg, D. Williams-Young, F. Ding, F. Lipparini, F. Egidi, J. Goings, B. Peng, A. Petrone, T. Henderson, D. Ranasinghe, V. G. Zakrzewski, J. Gao, N. Rega, G. Zheng, W. Liang, M. Hada, M. Ehara, K. Toyota, R. Fukuda, J. Hasegawa, M. Ishida, T. Nakajima, Y. Honda, O. Kitao, H. Nakai, T. Vreven, J. A. Montgomery, Jr., J. E. Peralta, F. Ogliaro, M. Bearpark, J. J. Heyd, E. Brothers, K. N. Kudin, V. N. Staroverov, T. Keith, R. Kobayashi, J. Normand, K. Raghavachari, A. Rendell, J. C. Burant, S. S. Iyengar, J. Tomasi, M. Cossi, J. M. Millam, M. Klene, C. Adamo, R. Cammi, J. W. Ochterski, R. L. Martin, K. Morokuma, O. Farkas, J. B. Foresman, and D. J. Fox, *GAUSSIAN 16*, Revision B.01, Gaussian, Inc., Wallingford, CT, 2016.
- ⁴⁵M. K. Kesharwani, B. Brauer, and J. M. L. Martin, *J. Phys. Chem. A* **119**, 1701 (2015).
- ⁴⁶J. Zheng, Y. Zhao, and D. G. Truhlar, *J. Chem. Theory Comput.* **5**, 808 (2009).
- ⁴⁷R. A. Marcus and O. K. Rice, *J. Phys. Chem.* **55**, 894 (1951).
- ⁴⁸T. Beyer and D. Swinehart, *Commun. ACM* **16**, 379 (1973).
- ⁴⁹G. da Silva, *J. Phys. Chem. A* **121**, 2086 (2017).
- ⁵⁰V. A. Mozhaevskiy and A. I. Krylov, ezSpectrum3.0, iOpenShell Center for Computational Studies of Electronic Structure and Spectroscopy of Open Shell and Electronically Excited Species, Los Angeles, <http://iopenshell.usc.edu/downloads>.
- ⁵¹M. J. Frisch, G. W. Trucks, H. B. Schlegel, G. E. Scuseria, M. A. Robb, J. R. Cheeseman, G. Scalmani, V. Barone, V. Mennucci, G. A. Petersson, H. Nakatsuji, M. Caricato, S. Li, H. P. Hratchian, A. F. Izmaylov, J. Bloino, G. Zheng, J. L. Sonnenberg, M. Hada, M. Ehara, K. Toyota, R. Fukuda, J. Hasegawa, M. Ishida, T. Nakajima, Y. Honda, O. Kitao, H. Nakai, T. Vreven, J. A. Montgomery, Jr., J. E. Peralta, F. Ogliaro, M. Bearpark, J. J. Heyd, E. Brothers, K. N. Kudin, V. N. Staroverov, T. Keith, R. Kobayashi, J. Normand, K. Raghavachari, A. Rendell, J. C. Burant, S. S. Iyengar, J. Tomasi, M. Cossi, N. Rega, J. M. Millam, M. Klene, J. E. Knox, J. B. Cross, V. Bakken, C. Adamo, J. Jaramillo, R. Gomperts, R. E. Stratmann, O. Yazyev, A. J. Austin, R. Cammi, C. Pomelli, J. W. Ochterski, R. L. Martin, K. Morokuma, V. G. Zakrzewski, G. A. Voth, P. Salvador, J. J. Dannenberg, S. Dapprich, A. D. Daniels, O. Farkas, J. B. Foresman, J. V. Ortiz, J. Cioslowski and D. J. Fox, *GAUSSIAN 09*, Revision B.01, Gaussian, Inc., Wallingford, CT, 2009.
- ⁵²M. P. Andersson and P. Uvdal, *J. Phys. Chem. A* **109**, 2937 (2005).
- ⁵³R. D. Levine, *Molecular Reaction Dynamics* (Cambridge University Press, New York, 2005).
- ⁵⁴R. H. Dalitz, *London, Edinburgh, Dublin Philos. Mag. J. Sci.* **44**, 1068 (1953).
- ⁵⁵I. Ramphal, M. Shapero, C. Haibach-Morris, and D. M. Neumark, *Phys. Chem. Chem. Phys.* **19**, 29305 (2017).
- ⁵⁶M. Ryazanov, A. W. Harrison, G. Wang, P. E. Crider, and D. M. Neumark, *J. Chem. Phys.* **140**, 234304 (2014).
- ⁵⁷G. da Silva, A. J. Trevitt, M. Steinbauer, and P. Hemberger, *Chem. Phys. Lett.* **517**, 144 (2011).
- ⁵⁸C. Maul and K.-H. Gericke, *Int. Rev. Phys. Chem.* **16**, 1 (1997).